This article has been accepted for publication in a future issue of this journal, but has not been fully edited. Content may change prior to final publication. Citation information: DOI 10.1109/TIE.2022.3169840, IEEE Transactions on Industrial Electronics

A Novel Efficient Hybrid Compensation Topology for Wireless Power Transfer

Saman Rezazade, Amir Shahirinia, *Senior Member, IEEE*, Reza Naghash, Navid Rasekh, *Student Member, IEEE*, Seyed Ebrahim Afjei, *Member, IEEE*

***Abstract*—Wireless power transfer systems require compensators to improve efficiency by increasing transfer power between transmitter and receiver. The most commonly used compensators are Series-Series, Series-Parallel, and Double-Sided LCC. This paper analyzes the comparison between typical compensators focusing on transfer efficiency. Due to these characteristics of typical compensators, a hybrid compensation topology is designed based on two compensators. Hybrid compensation topology is capable of switching between Series-Series and Double-Sided LCC topologies. Two AC switches are used on the transmitter and receiver for switching mode in hybrid compensation topology with wireless communication links, and its variation algorithm is clarified. A novel compensation topology guarantees system's efficiency for a wide range of loads based on the maximum efficiency of two compensation topologies. The possibility of a proposed hybrid compensator is verified with an experimental prototype used for massive vehicles.**

***Index Terms*—Wireless power transfer (WPT), Double-Sided LCC, hybrid compensator, T equivalent model, Optimization**

I. Introduction

WIRELESS power transfer (WPT) using the magnetic resonant concept was firstly proposed by Nikola Tesla. WPTs have been widely studied due to their low maintenance advantages, high reliability, flexibility, safety, and environment-friendly features [1]. WPTs have been used to supply power and many other applications such as cell phones, medical implants, electric vehicles, underwater power supplies, and so on [2]. There are different categories of Electric Vehicles (EV), namely, large or small, heavy or light. EVs include electric buses, electric vans, electric cars, and electric bicycles, some of which are popular in North American and European countries [2]. One of the critical issues about electric vehicles is their wireless charging which has made many researchers carry out this subject. Nowadays, EVs' charging system is playing a crucial role in EVs' progress [1]. It takes more time to refuel EVs than gasoline engine vehicles, and their charging stations are limited. Currently, EVs are charged using extended plugging cables to connect the battery package, which is difficult to handle [2], [3]. WPT technologies are an effective way to avoid concerns such as implementation, management of batteries installed in an electric vehicle, etc [4]. and can solve charging issues by increasing home charge stations [1], [5]. WPT can charge a battery of EVs from several millimeters to a few hundred millimeters distance at various power levels [5]. This system transfers energy from the transmitter coil to the receiver coil based on near-field electromagnetic and nonradiative.

Research on WPT technology has been extending since various applications needed increasing intervals between transmitter and receiver. These studies would have different fields such as compensation topology and circuit analysis [6], coil design techniques for larger coupling coefficient [7], optimization for high efficiency [8] and [9], control methods [10]-[12], peripheral object detection, and safety issues [13]. Compensation topology and circuit analysis are important because they determine resonant frequency, power factor, output characteristics, regulate resonant frequency, and minimize the VA rating of power supply [14]-[16]. The WPT system has four fundamental topologies, namely, Series-Series (SS), Series-Parallel (SP), Parallel-Parallel (PP), and Parallel-Series (PS). The first letter represents the primary coil's compensation, while the second letter represents the secondary coil's compensation.

Each of the topologies has several advantages and disadvantages. The SS topology has two capacitors on each side so that the capacitors are in series with the coils. This topology is applicable more than other types due to its simplicity to implement [17]-[19]. The SS compensation topology has the characteristic that the resonant frequency is independent of the coupling coefficient and load. More voltage stress across capacitors and more current stress across converter switches are the main limitations for SS compensation topology [18], [19]. The SS topology has less efficiency at lower load levels than other topologies [19]. The PP topology has a simple structure, which is composed of two coupling coils and two capacitors that are parallel to the coils. This topology requires current-fed inverters and supports the output short circuit [20]-[22]. The PP topology has less efficiency than the SS topology. On the contrary, the PP model can relieve efficiency's descent rate, but the load's power supply is relatively low. The primary side capacitance in PS topology depends on the output load and magnetic coupling, and with an inverter feed, that needs to have an additional inductor [21], [22]. At the same time, it increases the cost and size of the converter [20]. The SP topology is appropriate for a device's charge via magnetic coupling between transmitter and receiver [24]. It is a proper

S. Rezazade is with the Electrical Engineering, Shahid Beheshti University, Velenjak, Tehran, Iran. E-mail: sa.rezazade@mail.sbu.ac.ir

A. Shahirinia is with the faculty of Electrical and Computer Engineering Department, University of the District of Columbia, Washington, United States. E-mail: amir.shahirinia@udc.edu

R. Naghash is with the Electrical Engineering, Shahid Beheshti University, Velenjak, Tehran, Iran. E-mail: r.naghash@mail.sbu.ac.ir

N. Rasekh is with the Electrical Engineering, University of Bristol, Bristol, United Kingdom. E-mail: Navid.Rasekh@Bristol.ac.uk

S. E. Afjei is with the faculty of Electrical Engineering, Shahid Beheshti University, Velenjak, Tehran, Iran. E-mail: e-afjei@sbu.ac.ir

This article has been accepted for publication in a future issue of this journal, but has not been fully edited. Content may change prior to final publication. Citation information: DOI 10.1109/TIE.2022.3169840, IEEE Transactions on Industrial Electronics

topology for high-power applications. The SP compensation topology is not suited for a variation of the coupling coefficient because the gap and misalignment between two coils change in different applications [20]. The LCC compensation topology has been recently used in WPT systems that consist of one series inductor and two capacitors on each side. An integrated LCC compensation topology can achieve a unity power factor at the secondary side because it compensates for reactive power [25]-[28]. Meanwhile, zero current switchings could be performed when the compensator's parameter is tuned [28]. Several research studies have been done on the WPT systems' efficiency since it is an essential issue in the design and implementation.

This research focuses on increasing WPT systems' efficiency by proposing a new hybrid topology that combines the SS and double-sided LCC topologies due to their advantages, and they are suitable for the same load range. The proposed system can utilize the SS topology in the high load and double-sided LCC in the low load based on the determined control algorithm. Therefore, the proposed system has high efficiency for a variety of loads. Furthermore, the control function achieves boundary load and the controller switches between the two topologies, and the system structure changes at boundary load.

II. THEORETICAL ANALYSIS

This theoretical analysis includes two topologies for the WPT system: 1) Double-Sided LCC 2) SS , both of which are used for medium power levels. In WPT systems, two inductors are placed as primary and secondary coils. These two inductors are coupled to each other by mutual inductance M, the value of which will change according to the distance between the primary and secondary coils. Instead of using the M parameter, the coupling factor, k, can be used, which can be calculated based on the values of the coils and the mutual inductance.

A. Double-Sided LCC Compensation Topology

Fig. 1 shows the Double-sided LCC compensator topology. This compensator is more complex than the SS compensator, and this compensator has two more series inductors and two more parallel capacitors than that of the SS. Therefore, on the primary and secondary sides of this compensator there are two inductors and two capacitors. On the primary side, the voltage-fed inverter feeds the compensator circuit and the primary side coil. Therefore, inductors L_{f1} and L_{f2} with primary and secondary coils are not coupled in this compensator, and only the two primary and secondary primary coils are coupled to each other. With these interpretations in the Double-Sided LCC compensator circuit, there is only one value for coupling factor or cross-inductance. A constant operating frequency in this compensator is obtained from the following equations to obtain the design parameter.

$$(L_{fi}C_{fi})_{i=1,2} = (L_P - L_{f1})\,C_1 = (L_S - L_{f2})\,C_2 = \frac{1}{\omega_r^2} \tag{1}$$

As stated in the previous section, Kirchhoff's laws are used to obtain the voltage and current of the circuit. First, the

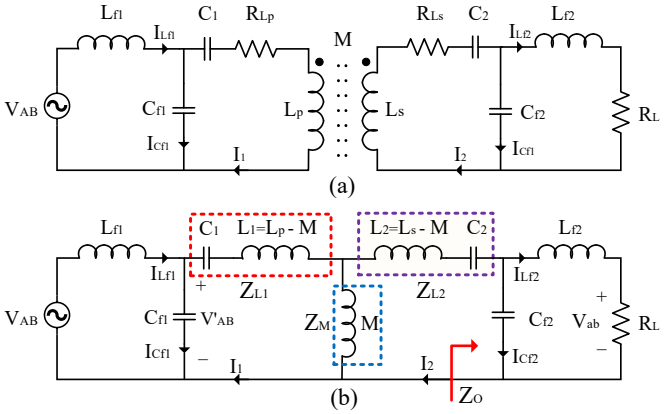

Fig. 1. (a) Double-Sided LCC compensated topology and (b) T equivalent model.

primary and secondary impedances must be determined. To do this we use the KVL of double-sided LCC topology:

$$\begin{aligned} &-\vec{V}_{AB}^{'} + (Z_{L1} + Z_M)\vec{I}_1 - Z_M I_2 = 0 \\ &(Z_{L2} + Z_M + Z_O)\vec{I}_2 - Z_M I_1 = 0 \\ &-\vec{V}_{AB} + Z_{L_{f1}}\vec{I}_{L_{f1}} + \vec{V}_{AB}^{'} = 0 \end{aligned} \tag{2}$$

where V_{AB} is the input voltage for the primary side circuit of the compensator and I_1 is the current on the primary side and I_2 is the current on the secondary side. Also, $Z^{'} = (Z_{L_{f2}} + R_L)||Z_{C_{f2}}$, where R_L is equivalent to AC resistance load that $R_L = \frac{8}{\pi^2}R_o$, which is the dc load of the system.To simplify circuit analysis, the inductance resistors L_{f1} and L_{f2} have been ignored. According to (2), the input and output currents are obtained as follows:

$$\begin{aligned} \vec{I}_{L_{f1}} &= \frac{(Z_{C_{f1}}(Z_{L2}+Z_O+Z_M)+X)\,\vec{V}_{AB}}{Y} \\ \vec{I}_{L_{f2}} &= \frac{(Z_{C_{f2}}Z_M)(Z_{C_{f1}}(Z_{L2}+Z_O+Z_M))\,\vec{V}_{AB}}{(Z_{C_{f2}}+Z_{L_{f2}}+R_L)(Z_{L2}+Z_O+Z_M)Y} \end{aligned}$$

$$\begin{aligned} X &= Z_{L1}(Z_{L2} + Z_M + Z_O) + Z_M(Z_{L2} + Z_O) \\ Y &= Z_{C_{f1}}Z_{L_{f1}}(Z_{L2} + Z_M + Z_O) + X(Z_{C_{f1}} + Z_{L_{f1}}) \end{aligned} \tag{3}$$

According to Equation (3), the voltage and current gains between the output and input are as follows:

$$\begin{aligned} G_V &= \frac{V_O}{V_{AB}} = \frac{R_L Z_O}{\frac{(SL_{f2}+R_L)(Z_{L2}Z_O)}{1+S^2L_{f1}C_{f1}+Z_{L1}(1+S^2L_{f1}C_{f1})+ASL_{f1}}} \\ G_I &= \frac{I_{L_{f2}}}{I_{L_{f1}}} = \frac{S^2MC_2}{(SC_{f1}W+1)T} \end{aligned} \tag{4}$$

$$A = \frac{SM+Z_{L2}Z_O}{SM(Z_{L2}Z_O)}$$

where $S = j\omega_r$. The frequency response of the Double-Sided LCC compensator obtained using the voltage gain is shown in Fig. 2. According to the voltage gain magnitude, this compensator can have two resonant frequencies, of which only one is considered according to Equation (1). According to Equation (3), the output power of this compensator is as follows:

This article has been accepted for publication in a future issue of this journal, but has not been fully edited. Content may change prior to final publication. Citation information: DOI 10.1109/TIE.2022.3169840, IEEE Transactions on Industrial Electronics

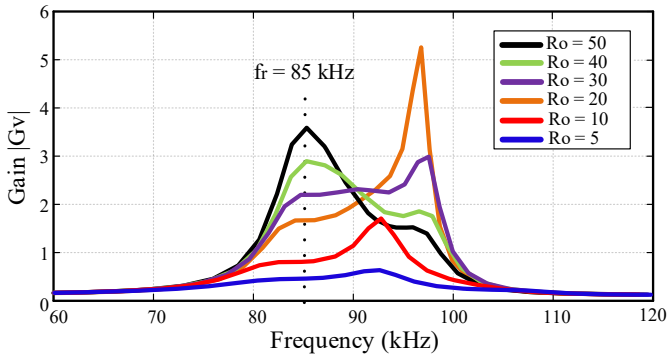

Fig. 2. Frequency responses of the double-sided LCC compensation topology to the load variation.

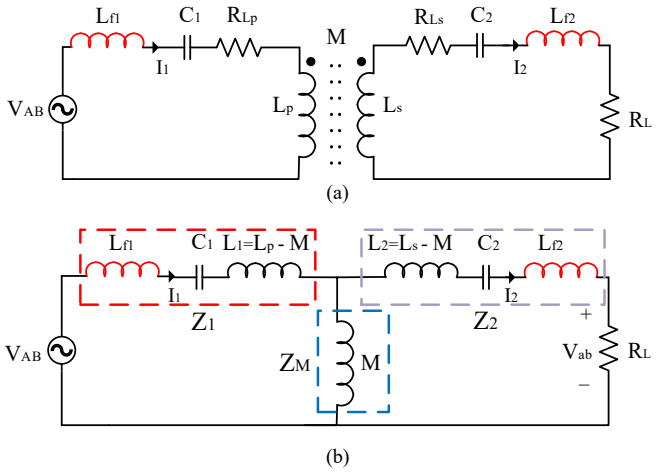

Fig. 3. (a) The SS compensation topology and (b) The T equivalent model.

$$P_{O_{LCC}} = R_L\left|\vec{I}_{Lf2}\right|^2 = \frac{R_L(MI_1)^2}{(R_{Ls}R_LC_{f2}+L_{f2})^2} \tag{5}$$

To calculate the efficiency of the LCC compensator, the power loss must be obtained on both sides of the network. According to relations (1), (2), (3) and (5), the efficiency of the double-sided LCC topology is obtained:

$$\eta_{LCC} = \frac{1}{1+\frac{R_{Lp}(R_{Ls}R_LC_{f2}+L_{f2})^2+R_{Ls}(R_LC_{f2}\omega_rM)^2}{(M)^2R_L}} \tag{6}$$

According to Equation (6), the values of C_{f2} and L_{f2} are essential for higher efficiency. Additionally, as the R_L value increases, the system efficiency decreases, but it should be noted that the slope of the efficiency reduction based on the R_L increase in the Double-Sided LCC compensator is less than that of the SS compensator. If $(\frac{L_{f2}}{C_{f2}})^{\frac{1}{2}}$ has a value slightly close to zero, the efficiency of this compensator depends on the term $(C_{f2}\omega_r)^2R_L$, and as a result, as the value of R_L increases, the rate of decrease in efficiency will decrease.

B. SS Compensation Topology

Fig. 3 shows the SS compensation topology. To simplify the analysis, the amount of parasitic resistance of capacitors and inductors is ignored. To analyze this compensator used in WPT systems, the T model is used as less complex than other models. The parameters of Model T are calculated below:

$$\begin{aligned} Z_1 &= j\omega_rL_{f1} + \frac{1}{j\omega_rC_1} + j\omega_rL_1 \\ Z_2 &= j\omega_rL_{f2} + \frac{1}{j\omega_rC_2} + j\omega_rL_2, Z_M = j\omega_rM \end{aligned} \tag{7}$$

The Z_1 and Z_2 are the primary and secondary side impedances, and ω_r is the angular frequency. Kirchoff rules have been used to obtain voltage and current gain in this compensator.

$$\begin{aligned} -V_{AB} + (Z_1 + Z_M)I_1 - Z_MI_2 = 0 \\ (Z_M + Z_2 + R_L)I_2 - Z_MI_1 = 0 \end{aligned} \tag{8}$$

V_{AB} and I_1 are the fundamental harmonics of the inverter output voltage and current expressed as phasors. I_2 is the main harmonic of the output current on the secondary side, defined as a phasor, and R_L is also equivalent to the AC resistance load. The V_{AB} input voltage relation can be used to obtain the primary and secondary currents.

$$\begin{aligned} \vec{I}_1 &= \frac{(Z_M+Z_2+R_L)V_{AB}}{Z_1Z_2+(Z_1Z_2)Z_M+(Z_1Z_M)R_L} \\ \vec{I}_2 &= \frac{Z_MV_{AB}}{Z_1Z_2+(Z_1Z_2)Z_M+(Z_1Z_M)R_L} \end{aligned} \tag{9}$$

According to Equation (9), the voltage and current gains between the output and input are obtained:

$$\begin{aligned} G_V &= \frac{V_{ab}}{V_{AB}} = \frac{Z_MR_L}{Z_1Z_2+(Z_1+Z_2)Z_M+(Z_1+Z_M)R_L} \\ G_I &= \frac{I_o}{I_i} = \frac{Z_M}{Z_M+Z_2+R_L} \end{aligned} \tag{10}$$

where V_{ab} is the output voltage on the secondary side and while C_1 and C_2 are the resonance capacitors of the system, which are obtained as follows:

$$\omega_rC_1 = \frac{1}{\omega_r(L_P+L_{f1})}, \omega_rC_2 = \frac{1}{\omega_r(L_S+L_{f2})} \tag{11}$$

According to (10) and (11), the voltage and current gains can be expressed as follows:

$$G_V = \frac{R_L}{\omega_rM}, G_I = \frac{\omega_rM}{R_L} \tag{12}$$

The frequency response of the SS compensator topology based on (10) is shown in Fig. 4.

The switching frequency of SS is placed between two points with a constant voltage gain, so it has a higher gain than those points. According to Kirchoff's laws and Equation (9), the primary and secondary currents can be expressed as follows:

$$\begin{aligned} \vec{I}_1 &= \frac{(R_{L_s}+R_L)\,\vec{V}_{AB}}{R_{L_p}(R_{L_s}+R_L)+\omega_r^2M^2} \\ \vec{I}_2 &= \frac{j\omega_rM\vec{V}_{AB}}{R_{L_p}(R_{L_s}+R_L)+\omega_r^2M^2} \end{aligned} \tag{13}$$

The primary current is in phase with the inverter's output voltage; therefore, the power factor can become one on the primary side. Also, assuming that the rectifier power losses are ignored, from (13), the output current can be expressed as follows:

$$I_O = \frac{2\sqrt{2}}{\pi}|\vec{I}_2| \tag{14}$$

This article has been accepted for publication in a future issue of this journal, but has not been fully edited. Content may change prior to final publication. Citation information: DOI 10.1109/TIE.2022.3169840, IEEE Transactions on Industrial Electronics

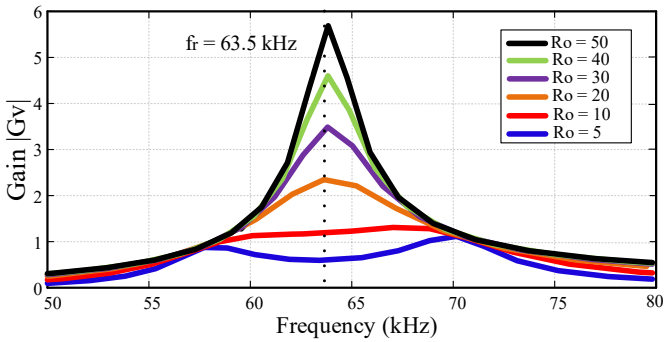

Fig. 4. Frequency response of the SS compensation topology to the load variation.

Where I_o is the rectifier output current. The output power is:

$$P_{O_{ss}} = R_L \left|\vec{I}_2\right|^2 = \frac{R_L(\omega_r M V_{AB})^2}{[R_{Lp}(R_{Ls}+R_L)+(\omega_r M)^2]^2} \tag{15}$$

The coil structure design is one of the critical parts of increasing power transmission. According to Equation (15), the output power will decrease with increasing load. To calculate the efficiency, the amount of power loss in both the primary and secondary directions must be calculated. To simplify the efficiency calculation, the inductance resistances of L_{f1} and L_{f2} have been omitted. Accordingly, concerning relationships (7), (8), (9), and (15), the efficiency value for a system with an SS compensator is calculated as follows:

$$\eta_{ss} = \frac{R_L(\omega_r M)^2}{R_{Lp}(R_{Ls}+R_L)^2+(R_{Ls}+R_L)(\omega_r M)^2} \tag{16}$$

R_{Ls} and R_{Lp} are constant, and the parameters R_L, M, and ω_r are variable. Given that $R_L >> R_{Ls}$, the value of $(R_{Ls} + R_L) \approx R_L$ and the efficiency are expected to change with changes in load and the amount of constant factor coupling between the primary and secondary coils. Given the efficiency relationship, the higher the R_L value, the lower the efficiency, which is an essential principle in the design of WPT systems.

Due to both efficiency equations (6) and (16), the boundary load for each coupling factor is obtained:

$$(R_L)^2\alpha_1 + R_L\alpha_2 + \alpha_3 = 0$$

$$\begin{aligned}
\alpha_1 &= R_{Lp} - R_{Ls}(\omega_{r,ss}\omega_{r,LCC}MC_{f2})^2 - R_{Lp}(R_{Ls}C_{f2}\omega_{r,ss}) \\
\alpha_2 &= 2R_{Lp}R_{Ls}(1-(\omega_{r,ss}^2 C_{f2}L_{f2})) \\
\alpha_3 &= R_{Lp}R_{Ls}^2 + R_{Ls}(\omega_{r,ss}M)^2 - R_{Lp}(\omega_{r,ss}L_{f2})^2
\end{aligned} \tag{17}$$

C. SWITCHED COMPENSATOR PROPOSED

Fig. 5 shows the proposed hybrid topology, which has a double-sided compensation network and two AC switches on each side. The Two AC switches on either side, the transmitter, and receiver are used to change the system's structure. Also, these switches can consist of two anti-parallel connected IGBTs or two anti-series connected MOSFETs. In our proposed structure, the MOSFET switch is used, as shown in Fig. 5 [19]. To change the structure of the compensator in the network, the output impedance after the rectifier must be measured first. To do this, the output voltage and current must be measured. Then the efficiency curve of each of the compensators should be obtained to achieve the boundary load. When the output impedance is measured, it is compared to the boundary R_b, and if it is less than that, the controller switches into the SS topology. Otherwise, it switches into the double-sided LCC topology.

For the system to be able to switch between two compensators, it needs a topology selector that will work based on the output voltage and current. Fig. 6 shows the block diagram of the topology selector. In this way, using the impedance detector measures the output voltage and current then, these are sent to the controller at the output to produce the desired pulse. In the main case, the AC switches on both ends, transmitter and receiver, must be in off-state simultaneously; otherwise, the voltage of capacitors C_{f1} and C_{f2} are peaky which will damage the system. So, the accuracy of the controller is paramount.Also, the output voltage is controlled by a single-loop output voltage controller and the PI controller generates the appropriate duty cycle value for inverter's switches.

III. EXPERIMENTAL RESULTS

Fig. 7 shows a 380-watt prototype based on the circuit shown in Fig. 5. Table I illustrates the parameters of the proposed system. Some of the measured parameters are slightly different from the designed values due to the tolerance of the components. The SS topology is obtained when parallel capacitors are eliminated from the circuit and the inductance of the inductors and coils remains constant. As a result, the SS topology resonance frequency is different from that of the LCC topology. In both mentioned topologies, the operating frequency of the system is set to the network resonance frequency. The transmitter and receiver coils are formed as a circle structure using Litz wire. The air gap between the two coils is $120mm$, based on which the coupling factor will be 26%.

To simplify the tests, an electric load has been used instead of the battery. During the test, an input voltage of $100V$ volts is considered.

TABLE I
WIRELESS CHARGER SPECIFICATIONS

Specification / Parameter	Value
Input DC voltage	100 V
Nominal gap	120 mm
Coupling coefficient	0.18 – 0.32
Primary coil inductance (L_P)	∼78.9 µH
Secondary coil inductance (L_S)	∼80 µH
Primary coil AC resistance	∼0.1 Ω
Secondary coil AC resistance	∼0.09 Ω
Series compensation inductance (L_{f1}, L_{f2})	∼23.6 µH
LCC Resonant capacitor (C_{f1}, C_{f2})	∼157.5 µF
Primary Series Resonant capacitor (C_1)	∼63.5 µF
Secondary Series Resonant capacitor (C_2)	∼60.5 µF
Switching Frequency (ω_{LCC})	85 kHz
Switching Frequency (ω_{SS})	63.5 kHz
Maximum power	∼380 W
Maximum efficiency	92.2 %

This article has been accepted for publication in a future issue of this journal, but has not been fully edited. Content may change prior to final publication. Citation information: DOI 10.1109/TIE.2022.3169840, IEEE Transactions on Industrial Electronics

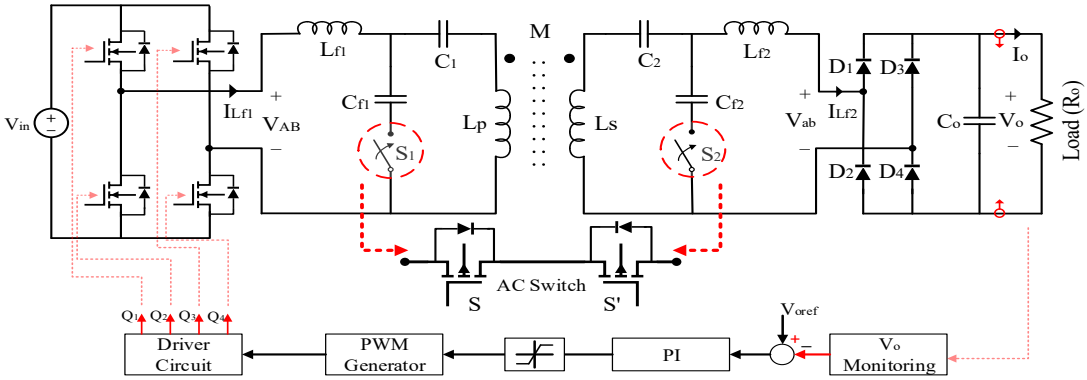

Fig. 5. Proposed hybrid topology with AC switches and control diagram.

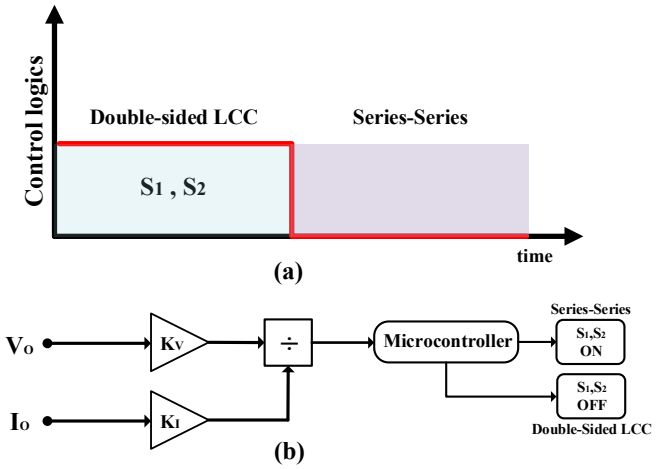

Fig. 6. (a) Control logic for AC switches and (b) Topology selector block diagram.

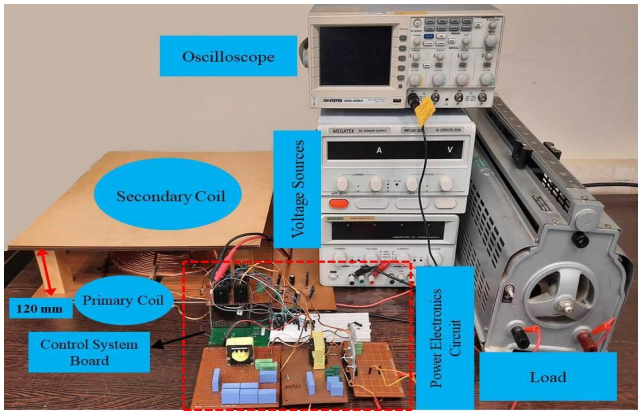

Fig. 7. The experimental lab prototype of the proposed system.

Inductance values are measured using an RLC meter and are consistent with the theoretical values intended for them. As mentioned, Equations (5) and (11) are used to calculate capacitor values. The current values $i_{C_{f1}}$ and $i_{C_{f2}}$ tend to zero after the AC switches are turned off, simultaneously, and the voltage across the capacitors increases to 250 volts. After the AC switches turn off, the primary side current will flow through the $L_{f1} - C_P - L_P$ path, and the secondary side current will flow through the $L_2 - C_S - L_{f2}$ path. Therefore, capacitors C_{f1} and C_{f2} are discharged and the voltage on them decreases, slowly. Therefore, the voltage of the primary and secondary coils increases because the values $\frac{di_P}{dt}$ and $\frac{di_S}{dt}$ are higher in the SS topology than that of LCC.

To measure the input and output parameters in both topologies, the load value has changed from 5Ω to 50Ω. When the S_1 and S_2 switches are turned off, the microcontroller changes the frequency from $85kHz$ to $63.5kHz$. Fig. 8 shows the total efficiency calculated based on the input power to the output power. According to Fig. 8, the R_b boundary load changes the system topology by the microcontroller and causes some system behavior to change. When the system uses the SS topology, the efficiency of the system should increase from 85.8% to 90.2% and finally reach 61.5% (when K=0.18). In this case, when the load is equal to the boundary load, the controller turns on the AC switches and the system will use the LCC topology because according to research, the lower the load, the greater the efficiency of the LCC topology compared to the SS topology [16], [25].

The experimental prototype was tested under three coupling factors of 0.18, 0.26, and 0.32, which are for $150mm$, $120mm$, and $100mm$ air gaps. Fig. 8(b) shows the efficiency of the system with a coupling factor of 0.26. By changing the air gap from $150mm$ to $120mm$, the coupling factor also changes to 0.26. As a result, with this change, the amount of boundary load, R_b, changes from 17Ω to 13Ω. According to Fig. 8(c), if the distance between two coils reduces to $100mm$, the coupling factor is 0.32, so under these circumstances, R_b is 11Ω. Fig. 8(d) shows the error bars of the system's efficiency, which is calculated for three coupling factors based on average output efficiency and load. The maximum error occurs at lower loads because the efficiency difference between the two topologies increases by reducing load. In addition, the prototype was tested under misalignment conditions. To do this, the secondary coil is moved along the x-axis from

This article has been accepted for publication in a future issue of this journal, but has not been fully edited. Content may change prior to final publication. Citation information: DOI 10.1109/TIE.2022.3169840, IEEE Transactions on Industrial Electronics

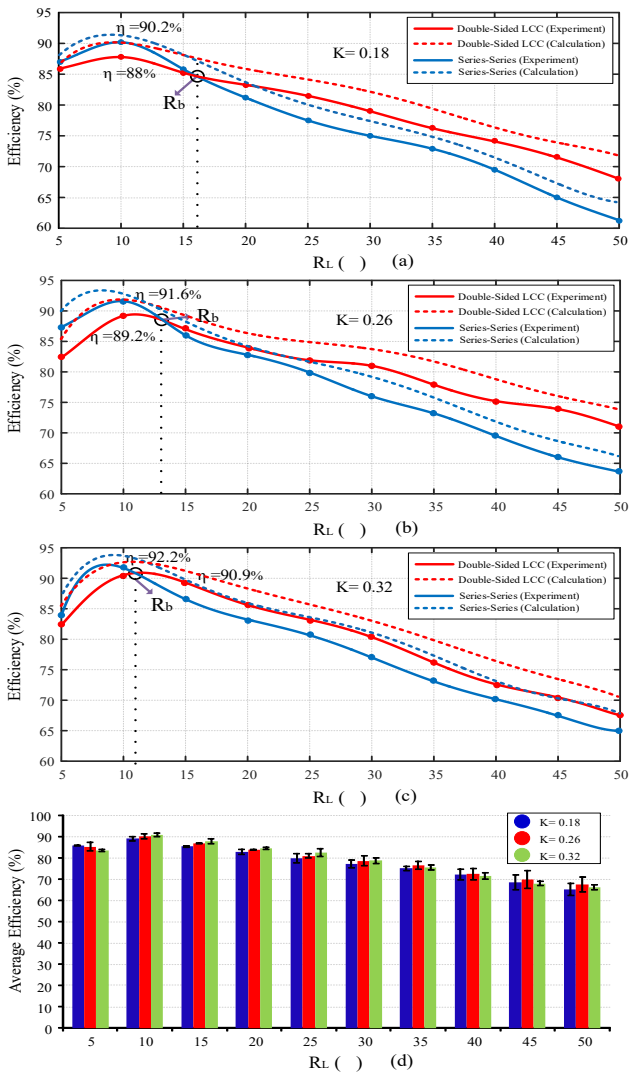

Fig. 8. Total efficiency of proposed topology and by coupling factor variation (a) $k = 0.18$, (b) $k = 0.26$, (c) $k = 0.32$ and (d) error bar of the average efficiency.

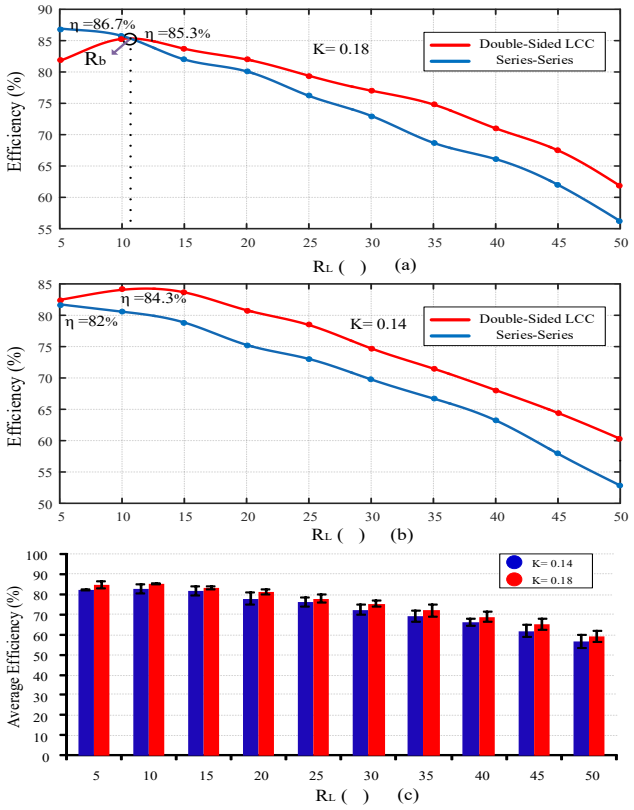

Fig. 9. Total efficiency of proposed topology with misaligns by coupling factor variation (a) $k = 0.18$, (b) $k = 0.14$ and (c) error bar of the average efficiency.

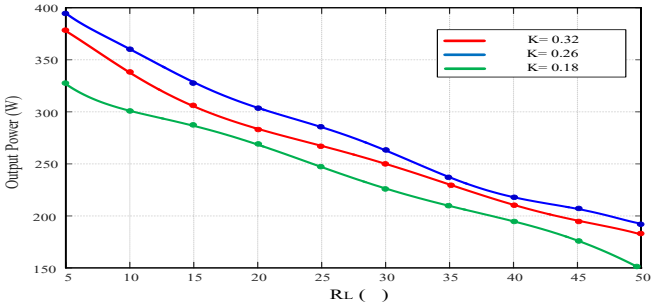

Fig. 10. The experimental output power of the proposed system.

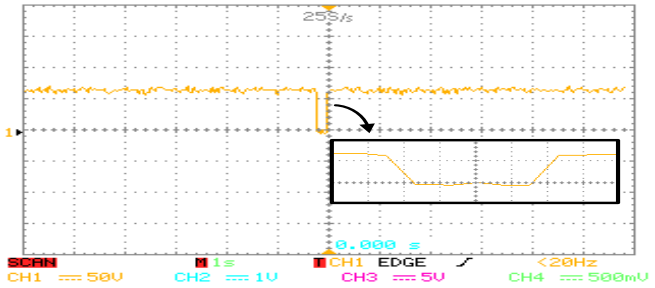

Fig. 11. DC output voltage for the double-sided LCC and the SS topology.

0 to $50mm$. Due to this change, the coupling factor has also changed to 0.18 and 0.14 for air gaps of $120mm$ and $150mm$. Fig. 9 shows the experimental efficiency of a system with different coupling factors under misalignment conditions.

The maximum efficiency of the system in the case of $50mm$ of misalignment and coupling factor of 0.18 is equal to 86.7%. In this case, the boundary load will also decrease. As the air gap increases, the coupling factor becomes 0.14, and the LCC efficiency will always be higher than the SS efficiency. Therefore, the system in this case will only use the LCC topology. According to Fig. 9(c), the error bars of the system's efficiency for the two coupling factors are achieved under the misalignment condition that the efficiency difference between the two topologies increases when the coupling factor is 0.14.

Fig. 10 shows the experimental output power of the proposed system for three coupling factors. The output power is equal for both topologies based on the constant output voltage controller. Due to the system's design process, the maximum output power is achieved when the coupling factor is 0.26. Also, the output power is shown for 0.18 and 0.32 and the out-

This article has been accepted for publication in a future issue of this journal, but has not been fully edited. Content may change prior to final publication. Citation information: DOI 10.1109/TIE.2022.3169840, IEEE Transactions on Industrial Electronics

put power reduces when the distance between the primary and secondary coils increases. Fig. 11 depicts that the controller achieves the output voltage's constant value. A single loop PI controller is used to sense the output voltage to achieve an accurate duty cycle in this system. After calculating output impedance by the microcontroller, when output impedance reaches R_b, in the first stage, the microcontroller turns off the MOSFET switches to change the system's topology. After changing the topology, the microcontroller turns on those switches (nearly 150 ms delay). This process avoids instability and current overshoot in the proposed system. Under these circumstances, when the load is less than the boundary load, the system's topology changes from series-series to double-sided LCC.

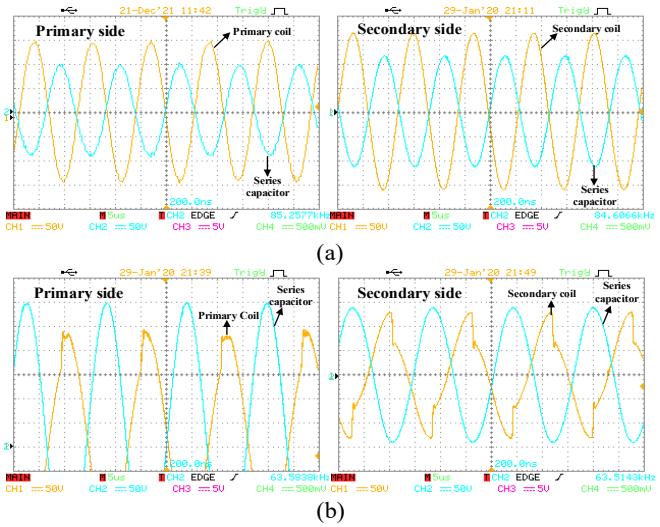

Fig. 12. Voltage of coils and series capacitors (a) the double-sided LCC topology (b) the SS topology.

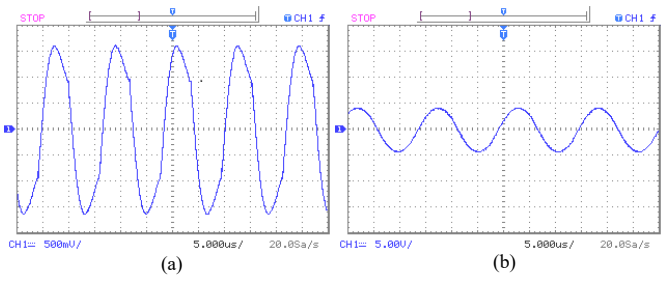

Fig. 13. Series inductance ($I_{L_{f1}}$) current (a) double-sided LCC topology (b) SS topology .

Fig. 12 shows the voltages of the coils and the series capacitors that are the same for both topologies. The coil voltage and voltage applied to the series capacitors are higher when the system operates with the SS topology than in the LCC topology. This is also because the primary and secondary coil currents are higher when the system operates with SS topology. The series inductance currents are also shown in Fig. 13. According to the $I_{L_{f1}}$ waveform, it is determined that the circuit operates near the resonant frequency, and the maximum possible power is transmitted between the primary and secondary.

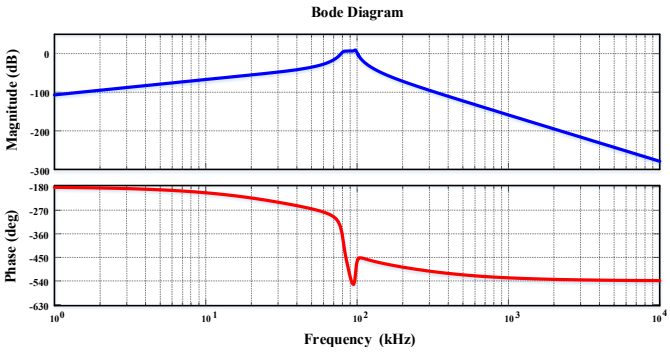

Fig. 14. Bode diagram of the SS topology.

IV. CONCLUSION

This paper combines the SS and double-sided LCC topologies to improve efficiency. The characteristics of these topologies will change as load resistance changes. Each of these topologies has unique characteristics that distinguish it from the other. Two compensation topologies make a hybrid topology using AC switches and a series inductance in the primary and secondary. When the load resistance changes and the system efficiency decreases, the controller switches by the AC switches according to the boundary load between the SS and the double-sided LCC topologies. The double-sided LCC topology is set for lower load and the SS topology for higher load in the desired hybrid topology. The controller receives the output feedback signals and specifies the impedance value for the control algorithm. Based on these feedback signals, the AC switches are controlled by this algorithm and make changes based on the set boundary load.

The coupling factor of the desired system in alignment and misalignment conditions varies between 0.14 and 0.32. The experimental results confirm the effectiveness of the proposed topology and illustrate its advantages as a high-efficiency charger in various applications. In addition, the experimental results show that the topology presented in the coupling factors and different loads has better efficiency than each of the topologies SS and double-sided LCC alone. In the future, the control system will be optimized to increase inverter efficiency by reducing losses and maintaining the output voltage constant.

V. APPENDIX

Fig. 14 and Fig. 15 show the bode plot of G_V, which contains both the double-sided LCC and the SS topology. These bode plots vary with changes in switching frequency for the load. Based on the structure design, the maximum magnitude is attained at the resonant frequency. The transfer functions of the double-sided LCC and the SS topologies are also obtained based on the proposed topology's parameters. Table II illustrates the transfer function parameters of the double-sided LCC topology.

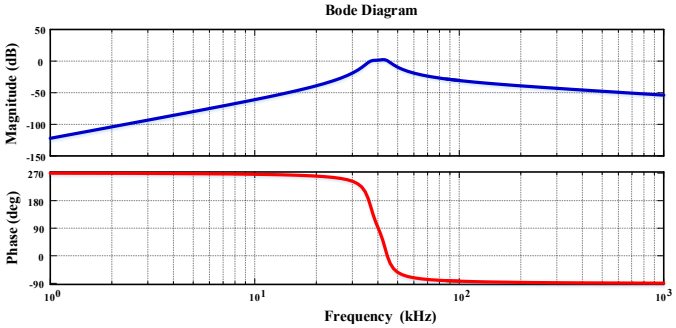

Fig. 15. Bode Diagram of the double-sided LCC topology.

$$G_{V_{SS}=}\frac{7.9e^{-19}S^3}{3.87e^{-23}S^4+3.94e^{-18}S^3+1.27e^{-11}S^2+6.36e^{-07}S+1} \tag{18}$$

$$G_{V_{LCC}} = \frac{A+B}{C+D+E+F}$$

$$\begin{aligned} A &= \mathrm{A}_1S^{11} + \mathrm{A}_2\mathrm{S}^{10} + \mathrm{A}_3S^9 + \mathrm{A}_4\mathrm{S}^8 + \mathrm{A}_5S^7 \\ B &= \mathrm{A}_6S^6 + \mathrm{A}_7S^5 + \mathrm{A}_8S^4 + \mathrm{A}_9S^3 + \mathrm{A}_{10}S^2 \\ C &= \mathrm{B}_1S^{17} + \mathrm{B}_2S^{16} + \mathrm{B}_3S^{15} + \mathrm{B}_4S^{14} + \mathrm{B}_5S^{13} \\ D &= \mathrm{B}_6S^{12} + \mathrm{B}_7S^{11} + \mathrm{B}_8S^{10} + \mathrm{B}_9S^9 + \mathrm{B}_{10}S^8 \\ E &= \mathrm{B}_{11}S^7 + \mathrm{B}_{12}S^6 + \mathrm{B}_{13}S^5 + \mathrm{B}_{14}S^4 + \mathrm{B}_{15}S^3 \\ F &= \mathrm{B}_{16}S^2 + \mathrm{B}_{17}S^1 + 2.37\mathrm{e}^{-18} \end{aligned} \tag{19}$$

TABLE II
THE COEFFICIENTS OF EQUATION 18.

coefficient	Value
A1	3.45e-83
A2	1.78e-76
A3	3.89e-70
A4	4.8e-64
A5	3.93e-58
A6	2.36e-52
A7	1.03e-46
A8	2.91e-41
A9	4.43e-36
A10	2.72e-31
B1	4.95e-116
B2	3.21e-109
B3	9.56e-103
B4	1.8e-96
B5	2.51e-90
B6	2.79e-84
B7	2.57e-78
B8	1.99e-72
B9	1.31e-66
B10	7.48e-61
B11	3.63e-55
B12	1.5e-49
B13	5.23e-44
B14	1.49e-38
B15	3.37e-33
B16	5.47e-28
B17	5.42e-23

REFERENCES

[1] Ahmad, M. S. Alam, and R. Chabaan, "A Comprehensive Review of Wireless Charging Technologies for Electric Vehicles," in IEEE Transactions on Transportation Electrification, vol. 4, no. 1, pp. 38-63, March 2018.

[2] Y. Li et al., "Efficiency Analysis and Optimization Control for Input-Parallel Output-Series Wireless Power Transfer Systems," in IEEE Transactions on Power Electronics, vol. 35, no. 1, pp. 1074-1085, Jan. 2020.

[3] G. Di Capua et al., "Mutual Inductance Behavioral Modeling for Wireless Power Transfer System Coils," in IEEE Transactions on Industrial Electronics, vol. 68, no. 3, pp. 2196-2206, March 2021.

[4] Y. Zhuang, A. Chen, C. Xu, Y. Huang, H. Zhao and J. Zhou, "Range-Adaptive Wireless Power Transfer Based on Differential Coupling Using Multiple Bidirectional Coils," in IEEE Transactions on Industrial Electronics, vol. 67, no. 9, pp. 7519-7528, Sept. 2020.

[5] C. Cheng et al., "A Load-Independent LCC-Compensated Wireless Power Transfer System for Multiple Loads With a Compact Coupler Design," in IEEE Transactions on Industrial Electronics, vol. 67, no. 6, pp. 4507-4515, June 2020.

[6] L. Wu, B. Zhang and J. Zhou, "Efficiency Improvement of the Parity-Time-Symmetric Wireless Power Transfer System for Electric Vehicle Charging," in IEEE Transactions on Power Electronics, vol. 35, no. 11, pp. 12497-12508, Nov. 2020.

[7] M. Budhia, J. T. Boys, G. A. Covic, and H. Chang-Yu, "Development of a Single-Sided Flux Magnetic Coupler for Electric Vehicle IPT Charging Systems," IEEE Trans. Ind. Electron., vol. 60, no. 1, pp. 318–328, Jan. 2013.

[8] Z. Wei,W. Siu-Chung, C. K. Tse, and C. Qianhong, "Design for Efficiency Optimization and Voltage Controllability of Series-Series Compensated Inductive Power Transfer Systems," IEEE Trans. Power Electron., vol. 29, no. 1, pp. 191–200, Jan. 2014.

[9] M. Najjarzadegan, I. Ghotbi, S. J. Ashtiani, O. Shoaei, and M. Shahabadi, "Improved Wireless Power Transfer Efficiency Using Reactively Terminated Resonators," in IEEE Antennas and Wireless Propagation Letters, vol. 17, no. 5, pp. 803-807, May 2018.

[10] R. Naghash, S. M. M. Alavi, and S. E. Afjei, "Robust Control of Wireless Power Transfer Despite Load and Data Communications Uncertainties," in IEEE Journal of Emerging and Selected Topics in Power Electronics, 2020.

[11] S. Samanta and A. K. Rathore, "Small-Signal Modeling and Closed-Loop Control of a Parallel–Series/Series Resonant Converter for Wireless Inductive Power Transfer," in IEEE Transactions on Industrial Electronics, vol. 66, no. 1, pp. 172-182, Jan. 2019.

[12] P. Xuewei, A. K. Rathore, "Small-Signal Analysis of Naturally Commutated Current-Fed Dual Active Bridge Converter and Control Implementation Using Cypress PSOC", IEEE Trans. Veh. Technol., vol. 64, no. 11, pp. 4996-5005, Nov. 2015.

[13] Y. Cao and J. A. A. Qahouq, "Analysis and Evaluation of a Dual-Variable Closed-Loop Control of Power Converter With Wireless and Nonwireless Power Transfer," in IEEE Transactions on Industrial Electronics, vol. 66, no. 4, pp. 2668-2679, April 2019.

[14] W. Li, H. Zhao, S. Li, J. Deng, T. Kan, and C. C. Mi, "Integrated LCC Compensation Topology for Wireless Charger in Electric and Plug-in Electric Vehicles," in IEEE Transactions on Industrial Electronics, vol. 62, no. 7, pp. 4215-4225, July 2015.

[15] Rasekh N, Dabiri S, Rasekh N, Mirsalim M, Bahiraei M. Thermal analysis and electromagnetic characteristics of three single-sided flux pads for wireless power transfer. Journal of Cleaner Production. 2020 Jan 10;243:118561.

[16] B. M. Mosammam, N. Rasekh, M. Mirsalim and J. S. Moghani, "Comparative Analysis of the Conventional Magnetic Structure Pads for the Wireless Power Transfer Applications," 2019 10th International Power Electronics, Drive Systems and Technologies Conference (PEDSTC), 2019, pp. 624-628.

[17] Y. Zhang, T. Kan, Z. Yan, and C. C. Mi, "Frequency and Voltage Tuning of Series–Series Compensated Wireless Power Transfer System to Sustain Rated Power Under Various Conditions," in IEEE Journal of Emerging and Selected Topics in Power Electronics, vol. 7, no. 2, pp. 1311-1317, June 2019.

[18] S. Sinha, A. Kumar, B. Regensburger, and K. K. Afridi, "Active Variable Reactance Rectifier—A New Approach to Compensating for Coupling Variations in Wireless Power Transfer Systems," in IEEE Journal of Emerging and Selected Topics in Power Electronics, vol. 8, no. 3, pp. 2022-2040, Sept. 2020.

[19] Y. Guo, Y. Zhang, W. Zhang and L. Wang, "Battery Parameter Identification Based on Wireless Power Transfer System With Rectifier Load," in IEEE Transactions on Industrial Electronics, vol. 68, no. 8, pp. 6893-6904, Aug. 2021.
[20] J. Hou, Q. Chen, S. Wong, C. K. Tse, and X. Ruan, "Analysis and Control of Series/Series-Parallel Compensated Resonant Converter for Contactless Power Transfer," in IEEE Journal of Emerging and Selected Topics in Power Electronics, vol. 3, no. 1, pp. 124-136, March 2015.
[21] C. Cheng, W. Li, Z. Zhou, Z. Deng and C. Mi, "A Load-Independent Wireless Power Transfer System With Multiple Constant Voltage Outputs," in IEEE Transactions on Power Electronics, vol. 35, no. 4, pp. 3328-3331, April 2020.
[22] Y.Zhang, Z. Yan, T. Kan, X. Zeng, S. Chen, and C. C. Mi, "Modeling and Analysis of a Strongly Coupled Series–Parallel-Compensated Wireless Power Transfer System," in IEEE Journal of Emerging and Selected Topics in Power Electronics, vol. 7, no. 2, pp. 1364-1370, June 2019.
[23] L. Tan, S. Pan, H. Liu, C. Xu, J. Guo, and X. Huang, "Load Detection Method for Multiple-Receiver Wireless Power Transfer Systems," in IET Power Electronics, vol. 10, no. 14, pp. 1951-1958, 17 11 2017.
[24] S. Cheapanich, C. Anyapo, and P. Intani, "Study of Wireless Power Transfer Using Series-Parallel Topology," 2017 International Electrical Engineering Congress (IEECON), Pattaya, 2017, pp. 1-4.
[25] S. Li, W. Li, J. Deng, T. D. Nguyen, and C. C. Mi, "A Double-Sided LCC Compensation Network and Its Tuning Method for Wireless Power Transfer," in IEEE Transactions on Vehicular Technology, vol. 64, no. 6, pp. 2261-2273, June 2015.
[26] C. Liao, J. Li, and S. Li, "Design of LCC Impedance Matching Circuit for Wireless Power Transfer System Under Rectifier Load," in CPSS Transactions on Power Electronics and Applications, vol. 2, no. 3, pp. 237-245, Sept. 2017.
[27] Y. Zhang, Z. Yan, T. Kan, Y. Liu, and C. C. Mi, "Modelling and Analysis of The Distortion of Strongly-Coupled Wireless Power Transfer Systems With SS and LCC–LCC Compensations," in IET Power Electronics, vol. 12, no. 6, pp. 1321-1328, 29 5 2019.
[28] U. Pratik, B. J. Varghese, A. Azad, and Z. Pantic, "Optimum Design of Decoupled Concentric Coils for Operation in Double-Receiver Wireless Power Transfer Systems," in IEEE Journal of Emerging and Selected Topics in Power Electronics, vol. 7, no. 3, pp. 1982-1998, Sept. 2019.

Saman Rezazade received a B.Sc. degree in electrical engineering from Arak University of Technology, Arak, Iran, in 2015, and an M.Sc. degree in electrical engineering from Shahid Beheshti University, Tehran, Iran, in 2018. He is currently a research assistant at the power electronics and motor drives research laboratory at Shahid Beheshti University. His research interests are designing and controlling high-power electronics converters, wireless power transfer (WPT), motor drive, and finite element analysis (FEA).

Amir Shahirinia (SM'22) received the B.Sc. and M.Sc. degrees from the K. N. Toosi University of Technology, Tehran, Iran, in 2002 and 2005, respectively, and the Ph.D. degree from the University of Wisconsin-Milwaukee in Electrical Engineering in 2014. He has also performed postdoctoral studies with the power electronics group at Rockwell Automation (Allen Bradly) from 2014 to 2016. He is now an Assistant Professor with the Department of Electrical and Computer Engineering at the University of the District of Columbia (UDC), Washington, D.C. Dr. Shahirinia is the Smart Grids and Artificial Intelligence (SGAI) lab director. He is also the director of the Center of Excellence for Renewable Energy (CERE) at UDC. His research background encompasses the areas of power electronics, motor drives, and power systems and ranges from optimal planning of renewable energy grid integration systems (REGIS) to modeling and intelligent real-time control of REGIS, Bayesian statistics, and predictive modeling of the REGIS.

Reza Naghash received a B.Sc. degree in electrical engineering from Shahid Chamran University, Ahvaz, Iran, in 2016, and an M.Sc. degree in power electronics and electric machines from Shahid Beheshti University, Tehran, Iran, in 2019. His research interests include wireless power transfer, control in power electronics, electrodynamics, and finite element analysis.

Navid Rasekh (S'20) received the B.Sc. degree from the Kermanshah University of Technology, Kermanshah, Iran, in 2015 and the M.Sc. degree from the Amirkabir University of Technology, Tehran, Iran, in 2018, both in electrical engineering. He is currently working toward a Ph.D. degree with the Electrical Energy Management Group, University of Bristol, Bristol, U.K. His main research interests include designing and controlling the power electronic converters, power loss measurement of magnetic components, wireless power transfer (WPT), and finite element analysis (FEA).

Ebrahim S. Afjei (M'11) received the B.S. and M.S. degrees in electrical engineering from The University of Texas at Austin, Austin, TX, USA, in 1984 and 1986, respectively, and the Ph.D. degree from New Mexico State University, Las Cruces, NM, USA, in 1991. He is currently a Professor at the Department of Electrical Engineering, Shahid Beheshti University, Tehran, Iran. His current research interests include switched reluctance motor drives and power electronics.